Effect of Ce^{3+} substitution at *B* site on magnetic phase transitions in $CoCr_2O_4$ nanoparticles

P Mohanty, TJ Nkosi, ARE Prinsloo and CJ Sheppard

Cr Research Group, Department of Physics, University of Johannesburg, PO Box 524, Auckland Park
2006, Johannesburg, South Africa

E-mail: `pankajm@uj.ac.za`

Abstract. The present work investigates the role of Ce^{3+} substitution at the Cr^{3+} site on spiral ordering and other magnetic transitions in $Co(Cr_{0.95}Ce_{0.05})_2O_4$ nanoparticles. X-ray diffraction (XRD) studies of the sample calcined at 600 °C, revealed phase purity along with broadened diffraction peaks which are a signature of the size effect. The crystallite size (D) estimated from the XRD was 6.3 ± 0.6 nm. The average particle size calculated from the transmission electron microscopy (TEM) data was found to be $D_{TEM} = 8.4 \pm 0.5$ nm, corroborating the XRD results. Electron diffraction patterns confirm the crystalline nature of the nanoparticles having a bi-pyramidal shape. Magnetization as a function applied field shows an increase in coercivity as the temperature was decreased below the Curie temperature, T_C. Magnetization measured as a function of temperature indicated the ferrimagnetic behaviour, with $T_C = 92.5 \pm 0.5$ K (using the "knee-point method"). However, the lock-in temperature observed for the $Co(Cr_{0.95}Ce_{0.05})_2O_4$ nanoparticles, $T_L = 15 \pm 2$ K, is in agreement with that previously reported for pure $CoCr_2O_4$. Interestingly the spiral ordering was smeared by the substitution of Ce^{3+} at the Cr^{3+} site. The present work describes the impact of rare-earth Ce^{3+} ion substitution at the *B* site that can alter the exchange interaction in such a way that causes suppression of the spin spiral modulation.

1. Introduction

Broken inversion symmetry of the spin behaviour is observed in compounds that have a spiral ordering which leads to ferroelectricity [1]. $CoCr_2O_4$ is such a compound that has a complex conical-spiral spin ordering of ferrimagnetic nature that has a spontaneous magnetization [2]. This observed spiral ordering has been found to induce ferroelectric polarization [3]. The crystal structure of $CoCr_2O_4$ is cubic spinel, where tetrahedral *A* sites are occupied by Co^{2+} and the octahedral *B* sites by Cr^{3+} [2, 3]. Isotropic antiferromagnetic *A*-*B* and *B*-*B* exchange interactions (J_{AB} and J_{BB}) among the nearest neighbours with $J_{BB}/J_{AB} > 2/3$, gives the solution for the ferrimagnetic spiral ground state having the spins located on the conical surfaces [4, 5]. The properties of a ferrimagnetic (FiM) material can be understood by the combination ferromagnetic (FM) and antiferromagnetic (AFM) orderings [6]. The basic ordering of spins in the compound is AFM with unequal magnitudes that lead to a net FM order in the case of ferrimagnetic materials [6]. For $CoCr_2O_4$, the onset of ferrimagnetic transition occurs at $T_C = 93$ K, and subsequent lowering of the temperature leads to a cross-over to the conical spin state with a uniform and transverse spiral spin state possessing an incommensurate propagation vector at 26 K [3,7]. The lock-in transition occurs at T_L at a temperature of about 15 K, indicating the incommensurate to commensurate phase transition [8]. In a single crystal of $CoCr_2O_4$, the occurrence of ferroelectricity is concomitant with the conical spin modulation, which is also responsible for spontaneous magnetization [3]. Yamasaki et al. [3] confirmed the robust clamping between the ferromagnetic and ferroelectric domains leading to the multiferroic properties. Choi et al. [2] experimentally demonstrated the abrupt jump in polarization and change in the sign at T_L with variation in temperature or change in isothermal magnetization without altering its direction at T_L and keeping the sign of the spiral wave vector unaltered.

In order to further understand the observed low-temperature transitions, works have been reported on polycrystalline [9], nanoparticle [10-13] and thin film [14, 15] based $CoCr_2O_4$ samples. As the magnetic interaction strongly depends on the J_{AB} and J_{BB}, the effect of substituting either *A*-or *B*-site cations was found to be effective on the magnetic transitions at T_C, T_S and T_L when different cations were substituted either at Co or Cr sites. The role of Ni [15-17], Cu [18], Mn [19], Mg [20], Ge [21] substitution at Co site, and Fe substitution [22, 23] at Cr sites have been explored by several groups. However, the substitution of a rare earth cation in $CoCr_2O_4$ has not been investigated. In ferrites, with the formula $M(Fe_2O_4)$ where *M* is a metal that can form divalent bonds, it has been found that the addition of a small amount of rare-earth ions significantly modifies the structural, magnetic and electric properties, depending on the rare-earth dopant used and its concentration [24]. Rare-earth ions possess unpaired 4f electrons and strong spin-orbit coupling of angular momentum. The substitution of rare earth ions (*R*) into the $CoCr_2O_4$ at Cr site can result in *R*-Cr interaction (3*d*–4*f* coupling) that may lead to modification of magnetic properties similar to that observed in rare-earth doped ferrites [25]. Cerium is the most abundant rare-earth element belonging to the lanthanide series having an atomic number of 58, which exhibits catalytic properties because of the shielding of 5*p* and 4*d* electrons in the 4*f* orbital [26]. Cerium oxides demonstrate both 3+ and 4+ state that enables oxides of the form of CeO_2 and CeO_{2-x} [26]. Thus, substitution using rare-earth Ce^{3+} substitution in $CoCr_2O_4$ should be interesting to investigate that can manipulate the *R*-Cr^{3+} interaction. The present work, therefore, discusses the role of Ce^{3+} substitution at the Cr^{3+} site on the structure and magnetic properties of $CoCr_2O_4$.

2. Experimental

Powder samples of $Co(Cr_{0.95}Ce_{0.05})_2O_4$ were synthesized by sol-gel techniques [18]. In this process, stock solutions of 0.5 M cobalt nitrate ($Co(NO_3)_2{\cdot}6H_2O$), chromium nitrate ($Cr(NO_3)_3{\cdot}9H_2O$) and cerium chloride ($CeCl_3{\cdot}7H_2O$) were prepared. The desired amount of the aforementioned solutions was placed in a beaker and stirred for one hour in order to obtain a homogeneous mixture. After an hour, 40 ml of ethylene glycol was added and the solution was stirred for another hour using a magnetic stirrer, whereafter, the solution was allowed to rest for 24 hours. The solution was then heated to evaporate the liquid. The remaining residue in the beaker was dried on a hot plate to obtain the powder. The residue was crushed to a fine powder and subsequently calcined at 600 °C in a box furnace for one hour.

The crystal structure of the samples was analyzed using a PAN Analytical X-ray Diffractometer (XRD) with Cu-*K*α radiation ($\lambda = 1.54056$ Å). The microstructure of the calcined powder samples was studied using a JEM-2100 transmission electron microscope (TEM). Selected area electron diffraction (SAED) and energy-dispersive x-ray spectroscopy (EDS) of the samples were done using the same instrument. A 14 T Cryogen Free Physical and Magnetic Measurement System (CRYOGENIC Ltd., UK) with a vibrating sample magnetometer (VSM) insert was employed to carry out temperature and probing field-dependent magnetization measurements.

3. Results and discussion

Figure 1 (a) depicts the Rietveld refinement of the x-ray diffraction (XRD) pattern for the $Co(Cr_{0.95}Ce_{0.05})_2O_4$ sample using the GSAS II software package [27]. The broadening of the peaks and the low intensity related to the background are ascribed to the size effect [28]. However, the diffraction peaks related to the major (111), (220), (311), (222), (400), (422), (511), (440) and (533) reflections of the $CoCr_2O_4$ phase are distinct and could be labeled, as shown in Figure 1 (a). The lattice parameters and position coordinates obtained from the refinement are tabulated in Table 1. The ionic radius of Ce^{3+} in octahedral coordination is 1.101 Å compared to the Cr^{3+} ionic radii of 0.615 Å [29]. Even the large ionic radii of Ce^{3+} compared to Co^{2+} (0.58 Å) forces it to occupy the *B* sites. Because of the large ionic radii of Ce^{3+}, the solubility of it in a matrix having ions of smaller ionic radii will decrease [30]. The obtained lattice parameter of 8.321 Å (Table 1) is similar in value to the reported lattice parameter of

$CoCr_2O_4$ of 8.326 Å [31]. In addition, the effect of larger ionic radii of Ce^{3+} has been found to restrict crystal growth, and as a consequence, a reduction in the mean particle size was observed [30].

In order to estimate the average particle size and micro-strain, the Williamson-Hall (W-H) equation [32] was used:

$$\beta\cos\theta = \frac{K\lambda}{D} + 4\varepsilon\sin\theta, \quad (1)$$

where β the FWHM (full width at half maxima), K is the shape factor (taken as 0.6 considering spherical particles), λ is the x-ray wavelength and D is the average crystallite size and ε is the micro-strain induced in powders due to crystal imperfection and distortion [32]. Plotting ($\beta\cos\theta$) as a function of ($4\sin\theta$) as shown in Figure 1 (b) one can estimate ε and D from the slope and intercept, respectively. The calculated value of D is 6.3 ± 0.6 nm and the negative slope of the plot gives the value $\varepsilon = -0.002 \pm 0.001$. Negative values of ε ($-9.86 \times 10^{-4}$) were previously reported by Choudhary et al. [33] for $CoCr_2O_4$ nanoparticles. In the present case, adding Ce^{3+} is found to increase the strain. The occurrence of micro-strain also manifests a large surface-to-volume ratio and crystal field stabilization energy (CFSE) for the synthesized nanoparticles [33]. Nanoparticles which possess higher surface to volume ratio have a direct relationship between the average crystallite size and induced micro-strain [33]. The negative value of the strain is an indicative of compressive strain in the crystallites and nanoparticles [34]. Thus, it can be affirmed that 600 °C is sufficient for the particles' phase formation.

In order to obtain the particle size and determine the crystallinity of the particles, transmission electron microscopy (TEM) with selected area diffraction (SAED) and high-resolution electron microscopy (HREM) were used. Figure 2 (a) shows the TEM image of the nanoparticles. The particles are well dispersed but non-uniform in size, with sizes ranging between 5 nm to 45 nm. In Figure 3 (a) the particle size histogram is given, together with a log-normal fit [35]. The average particle size was obtained from the TEM images at various locations and is found to be 8.4 ± 0.5 nm. The average particle size corroborates the particle size obtained from the XRD results.

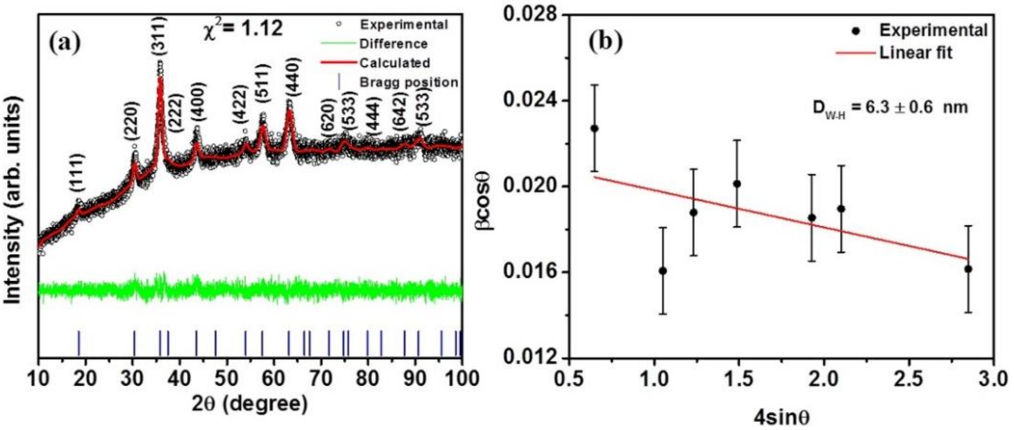

Figure 1. (a) Rietveld refinement of the XRD pattern of $Co(Cr_{0.95}Ce_{0.05})_2O_4$ nanoparticles, where the black symbols are the measured data and red the Rietveld refined fit. (b) Williamson-Hall (W-H) plot for the sample.

Table 1. Position coordinates obtained from the Rietveld refinement ($a = b = c$ = 8.32127 (Å), $\alpha = \beta = \gamma$ = 90, wR = 2.38 %, χ^2 = 1.12 and GOF = 1.06)

	***x*-coordinate (Å)**	***y*- coordinate (Å)**	***z*- coordinate (Å)**
Co	0.12500	0.12500	0.12500
Cr	0.50000	0.50000	0.50000
O	0.25176	0.25176	0.25176
Ce	0.50000	0.50000	0.50000

Distinct spots are observed in the SAED image, shown as an inset to Figure 2 (a), taken from particles in the image of Figure 2 (a), confirming the crystallinity of the particles. HREM image given in Figure 2 (b) clearly shows the lattice fringes and bi-pyramidal shape. The lattice fringes are labeled as (111) planes of the cubic lattice (see Figure 2 (b)), which is in agreement with the crystallite size. The presence of elements, especially the rare-earth Ce^{3+}, was confirmed by energy-dispersive x-ray spectroscopy (EDS), as shown in Figure 3 (b). The peaks related to Cu and C arise from the carbon-coated Cu-grid used for the imaging.

In order to explore the magnetic transitions, magnetization (zero field cooled (M_{ZFC}) and field cooled (M_{FC})) as a function of temperature was measured using an encapsulated sample with a probing field of 0.01 T; results are shown in Figure 4 (a). The irreversible temperature where M_{ZFC} and M_{FC} bifurcate, was found to be at 102 ± 2 K. The overall temperature behaviour of the Ce doped sample resembles that of $CoCr_2O_4$ [30]. A minimum in magnetization at $T = 15 \pm 2$ K in M_{FC} can be attributed to the T_L in the case of $CoCr_2O_4$. The feature related to spiral ordering which is observed at 26 K [3, 7] in $CoCr_2O_4$, is not observed in the present case. Zákutná et al. [13] found a critical size equal to 4.4 (1) nm above which spin-spiral can exist. A minimum spin-spiral period that can be accommodated in the nanoparticle of the size of 6.4 (1) nm has been reported by the same author [13]. In the present case, even though the particle size is above the critical size value, the absence of spiral ordering suggests the possible role of Ce^{3+} addition. W-H results already indicated a larger value of ε in the present case compared to the

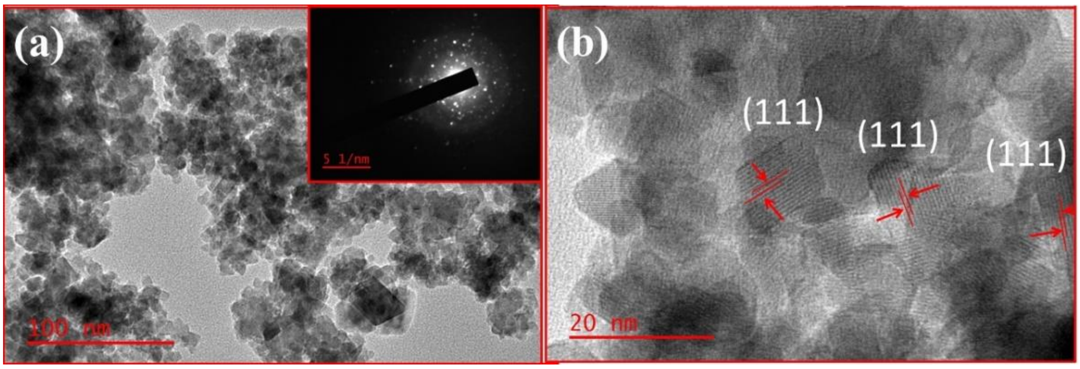

Figure 2. (a) TEM image of $Co(Cr_{0.95}Ce_{0.05})_2O_4$ nanoparticles (inset shows the SAED pattern) and (b) HR-TEM image of $Co(Cr_{0.95}Ce_{0.05})_2O_4$ nanoparticles showing lattice fringes related to (111).

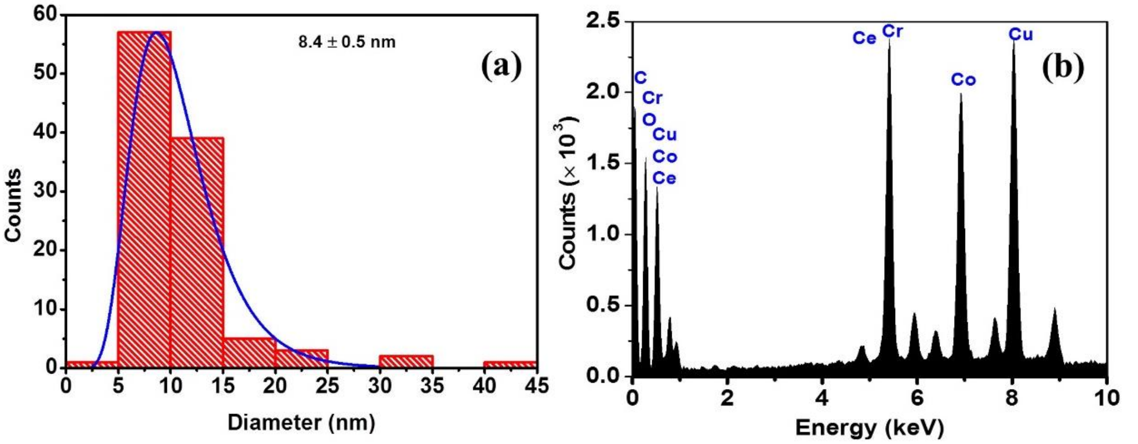

Figure 3. (a) Particle size histogram for $Co(Cr_{0.95}Ce_{0.05})_2O_4$ nanoparticles resulted from TEM imaging and (b) EDS results for $Co(Cr_{0.95}Ce_{0.05})_2O_4$ nanoparticles.

$CoCr_2O_4$ nanoparticles [33]. The disappearance of T_S was also noticed in epitaxial $CoCr_2O_4$ thin films, where the role of strain was significant [15]. In $CoCr_2O_4$ polycrystalline samples, applying external hydrostatic pressure up to 10 kbar using silicon oil as the pressure medium could only shift the T_S at a rate of about 0.1 K per kbar to high temperatures as a consequence of geometric frustration [36]. Hence, in the present case, the role of chemical pressure, created by doping an element chemically during the crystal formation, is found to be more dominant in alternating magnetic transitions.

Figure 4 (b) shows dM/dT plotted as function of temperature. The plot yields a minimum at 86.6 ± 0.3 K indicating the T_C (Figure 4 (b)). On the other hand, using the “knee-point method” as used earlier [17], the value of T_C is estimated to be 92.5 ± 0.5 (Figure 4 (c)). However, previous studies hinted that various methods to obtain T_C might be misleading, as in both methods, an external magnetic field was applied [31]. So far, the best method to find T_C is by neutron diffraction method, which is measured without any external magnetic field [31] that can be done in the future. Further, to understand deeper the $\Delta M = |M_{FC} - M_{ZFC}|$ as a function of temperature has been plotted in Figure 4 (d). This clearly shows the double slope of the difference in the magnetization curve just below the Curie temperature. This type of double slope feature in ΔM as a function of temperature was not observed in the case of Ni substituted $CoCr_2O_4$ [31]. It is important to note that rare-earth Ce metal has a magnetic ordering below 12.5 K along with a magnetic moment of 2.4 μ_B [37]. The absence of any transition around that temperature indicates the absence of Ce in metallic form in the present nanoparticles.

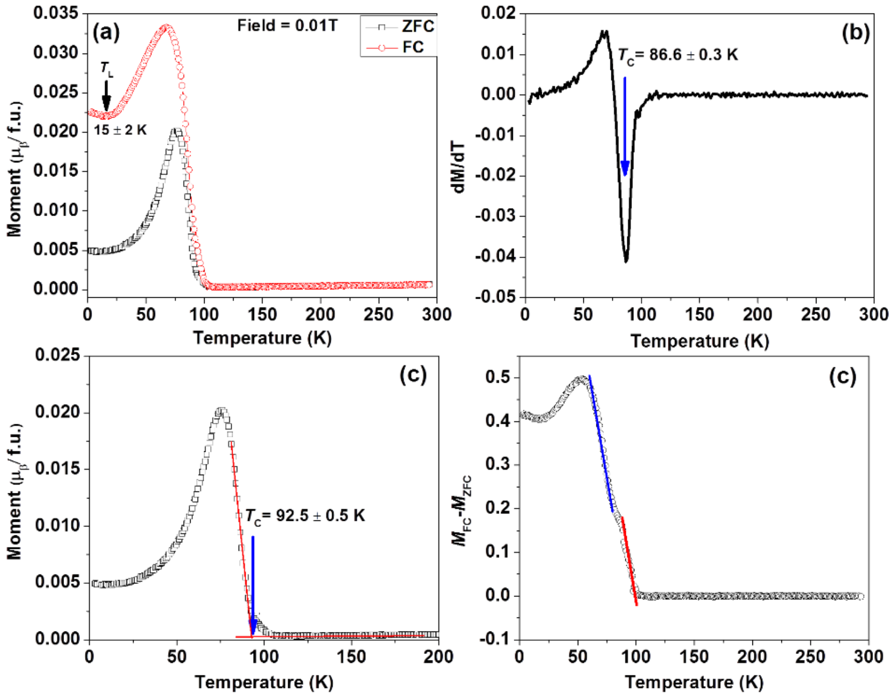

Figure 4. (a) Temperature-dependent magnetization measured with ZFC and FC protocols for $Co(Cr_{0.95}Ce_{0.05})_2O_4$ nanoparticles, (b) First order derivative of the ZFC magnetization data as function of temperature for $Co(Cr_{0.95}Ce_{0.05})_2O_4$ nanoparticles, (c) Estimation of T_C using knee-point method and (d) $\Delta M = |M_{FC} - M_{ZFC}|$ values as function of temperature for $Co(Cr_{0.95}Ce_{0.05})_2O_4$ nanoparticles.

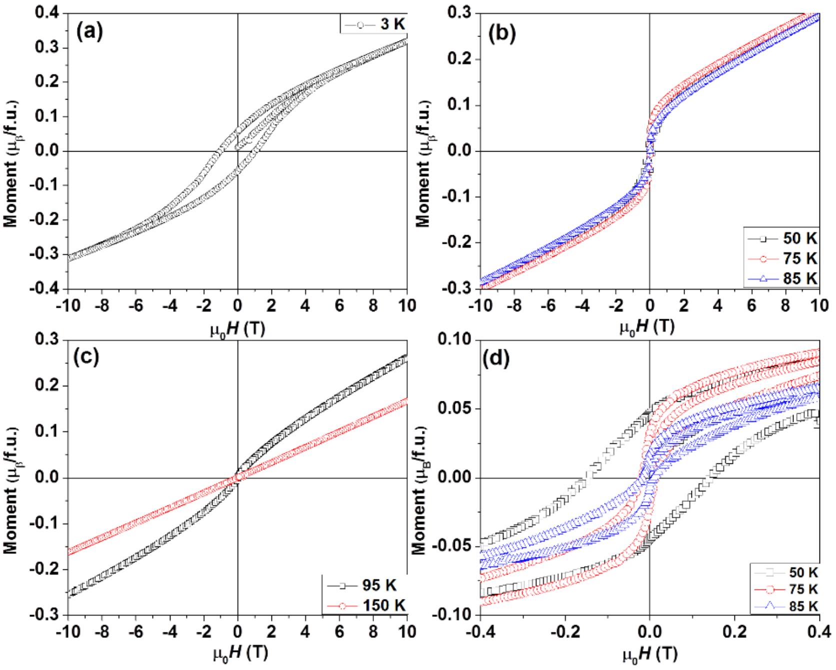

Figure 5. Magnetic field dependent magnetization measurement, $M(\mu_0 H)$, for $Co(Cr_{0.95}Ce_{0.05})_2O_4$ nanoparticles at (a) 3 K , (b) 50 K, 75 K and 85 K , (c) 95 K and 150 K , (d) Zoomed view around zero field regime for 50 K, 75 K and 85 K.

The magnetization as a function of magnetic field ($M(\mu_0 H)$) at constant temperature was performed at 3 K, 50 K, 75 K, 85 K, 95 K and 150 K. Figure 5 (a) shows the hysteresis loop measured at 3 K. The hysteresis loop reveals two observable kinks at field $\mu_0 H = \pm\ 2.3$ T. Figure 5 (b) shows the hysteresis loops measured at 50 K, 75 K and 85 K. The coercivity significantly decreased compared to the hysteresis loop measured at 3 K. The hysteresis loop suggests the presence of uncompensated spins at the surface that behave like a paramagnet giving rise to a linear increase in magnetization once the loop closes with increasing the applied field [11]. Figure 4 (c) shows the hysteresis loop measured at 95 K and 150 K. Persistence of hysteresis up to 95 K suggests the T_C value to be higher than that, contrary to the observed T_C obtained by the "knee-point method". However, at 150 K, the magnetization traces a linear curve indicative of paramagnetic nature, which is in accordance with the *M*-*T* results. In Figure 4 (d), the hysteresis loops are shown for measurements done at 50 K, 75 K and 85 K. The hysteresis loops appeared to be opened up above and below the zero applied field regime. The feature is most distinct for the loop measured at 75 K and 85 K (see Figure 4 (d)). Similar constricted loops were obtained in Ni substituted $CoCr_2O_4$ nanoparticles [18]. The appearance of the constricted hysteresis loop can be attributed to the various exchange interaction among the magnetic cations at different atomic sites [18]. Upon careful observation of the virgin curve (see Figure 4 (d)), an increase in magnetization with an applied magnetic field shows that the magnetization increases going from 50 K to 75 K and then reduces in the case of 85 K. Such anomalous behaviour can be linked to the temperature dependent magnetization as reflected in Figure 4 (a). Locating the magnetization values at 50 K, 75 K and 85 K in the M_{ZFC} plot can explain the abnormal increases and then decrease in magnetization in the hysteresis loops measured from 50 K to 85 K. The fundamental magnetic parameters such as saturation magnetization (M_S), remanence (M_R) and coercivity ($\mu_0 H_C$) obtained from the hysteresis loops are tabulated in Table 2. The squareness of the hysteresis loops can be estimated by the parameter M_r/M_s, which is also tabulated in Table 2. The obtained ratios less than 0.5 (except for 3 K) indicating magnetic multi-domains [38].

Table 2. Magnetic parameters obtained from temperature dependent hysteresis loops.

Temperature K	**M_s (μ_B/f.u.)**	**M_r (μ_B/f.u.)**	**$\mu_0 H_c$ (T)**	**Squareness (M_r/M_s)**
3	0.31	0.57	1.038	1.84
50	0.30	0.05	0.995	0.17
75	0.31	0.03	0.017	0.10
85	0.29	0.02	0.015	0.07
95	0.26	0.004	0.030	0.015

4. Conclusion

$Co(Cr_{0.95}Ce_{0.05})_2O_4$ nanoparticle samples were synthesized by a cost-effective sol-gel technique. The phase formation was achieved by calcining the powder samples at 600 °C. XRD confirms the phase purity, and the average crystallite was determined to be 6.3 ± 0.6 nm. Careful analysis of the TEM results indicated a non-uniform distribution of particle sizes with a mean particle size of 8.4 ± 0.5 nm, obtained from the log-normal distribution of the majority of bi-pyramidal structured grains. M_{ZFC} (T) and M_{FC} (T) measurements at low temperatures showed significant irreversibility and disappearance of spiral ordering as observed in the case of $CoCr_2O_4$. The low temperature hysteresis loops measured 50, 75 and 85 K showed the anomalous constricted nature of the loops around zero applied fields. Retention of the hysteretic behaviour up to 95 K clearly indicates the value of T_C beyond this value. The present work shows the potential impact of rare-earth Ce^{3+} ion substitution at the *B* site that can alter the exchange interaction in such a way that causes suppression of the spin modulation.

Acknowledgements

Financial aid from the SANRF (Grant No: 120856) and the UJ URC and FRC are acknowledged. The use of the NEP Cryogenic Physical Properties Measurement System at UJ, obtained with financial support from the SANRF (Grant No: 88080) and UJ, RSA, is acknowledged. The use of the Spectrum Analytical Facility in the FoS at UJ is conceded.

References

[1] Khomskii DI 2006 *J. Magn. Magn. Mater.* **306** 1-8

[2] Choi YJ, Okamoto J, Huang DJ, Chao KS, Lin HJ, Chen CT, Van Veenendaal M, Kaplan TA and Cheong SW. 2009 *Phys. Rev. Lett.* **102** 067601

[3] Yamasaki Y, Miyasaka S, Kaneko Y, He JP, Arima T and Tokura Y 2006 *Phys. Rev. Lett.* **96** 207204

[4] Lyons DH, Kaplan TA, Dwight K and Menyuk N 1962 *Phys. Rev.* **126** 540

[5] Menyuk N. Magnetism. In Modern Aspects of Solid State Chemistry 1970 (pp. 159-217). *Springer,* Boston, MA

[6] Majumdar K and Mahanti SD 2021 *J. Phys.: Condens. Matter* **33** 125801

[7] Dzyaloshinsky I 1958 *J. Phys. Chem. Solids* **4** 241-55

[8] Funahashi S, Morii Y and Child HR 1987 *J. App. Phys.* **61** 4114-6

[9] Lawes G, Melot B, Page K, Ederer C, Hayward MA, Proffen T and Seshadri R 2006 *Phys. Rev.* B **74** 024413.

[10] Dutta DP, Manjanna J and Tyagi AK 2009 *J. Appl. Phys.* **106** 043915

[11] Kumar L, Mohanty P, Shripathi T and Rath C 2009 *Nanosci. Nanotech. Lett.* **1** 199-203

[12] Zákutná D, Vlček J, Fitl P, Nemkovski K, Honecker D, Nižňanský D and Disch S 2018 *Phys. Rev.* B **98** 064407
[13] Zákutná D, Alemayehu A, Vlček J, Nemkovski K, Grams CP, Nižňanský D, Honecker D and Disch S 2019 *Phys. Rev.* B. **100** 184427
[14] Windsor YW et al 2017 *Phys. Rev.* B **95** 224413
[15] Mohanty P et al 2020 Nanotechnology **31** 285708
[16] Bush AA, Shkuratov VY, Kamentsev KE, Prokhorov AS, Zhukova ES, Gorshunov BP and Torgashev VI. 2012 *Phys. Rev.* B **85** 214112
[17] Mohanty P, Sheppard CJ, Prinsloo AR, Roos WD, Olivi L and Aquilanti G 2018 *J. Magn. Magn. Mater.* **451** 20-8
[18] Mohanty P, Sheppard CJ, Doyle BP, Carleschi E and Prinsloo AR 2021 *AIP Advances* **11** 025113
[19] Nadeem K, Rehman HU, Zeb F, Ali E, Kamran M, Noshahi NA and Abbas H 2020 *J. Alloys. Comp.* **832** 155031
[20] Rahman S, Saqib H, Zhang J, Errandonea D, Menéndez C, Cazorla C, Samanta S, Li X, Lu J and Wang L. 2018 *Phys. Rev.* B **97** 174102
[21] Hernández NO et al 2021 *Phys. Rev.* B **103** 085123
[22] Mohanty P, Prinsloo AR, Sheppard CJ and Roos WD 2018 *Acta Phys. Pol.* A. **133** 574-7
[23] Li CL, Yan TY, Barasa GO, Li YH, Zhang R, Fu QS, Chen XH and Yuan SL 2018 *Ceram. Intern.* **44** 15446-52
[24] Rahimi-Nasrabadi M, Behpour M, Sobhani-Nasab A and Jeddy MR 2016 *J. Mater. Sci: Mater Electron* **27** 11691-7
[25] Hashim M, Raghasudha M, Meena SS, Shah J, Shirsath SE, Kumar S, Ravinder D, Bhatt P, Kumar R and Kotnala RK 2018 *J. Magn. Magn. Mater.* **449** 319-27
[26] Singh KR, Nayak V, Sarkar T and Singh RP 2020 *RSC Adv* **10** 27194–27214
[27] Toby BH and Von Dreele RB 2013 *J. Appl. Cryst.* **46** 544-9
[28] Rath C, Mohanty P, Pandey AC and Mishra NC 2009 *J. Phys. D: Appl. Phys.* **42** 205101
[29] Shannon RD 1976 *Acta Crystallographica Section A* **32** 751-67
[30] Ghosh MP and Mukherjee S 2020 *J. Mater. Sci: Mater Electron* **31** 6207-16
[31] Mohanty P, Venter AM, Sheppard CJ and Prinsloo AR 2020 *J. Magn. Magn. Mater.* **498** 166217
[32] Mote VD, Purushotham Y and Dole BN 2012 *J. Theor. Appl. Phys.* **6** 1-8
[33] Choudhary P, Saxena P, Yadav A, Sinha AK, Rai VN, Varshney MD and Mishra A 2019 *J. Sup. Conduct. Nov. Magn.* **32** 2639-45
[34] Tripathi AK, Mathpal MC, Kumar P, Singh MK, Soler MA and Agarwal A 2015 *J. Alloy. Comp.* **622** 37-47
[35] Zákutná D, Repko A, Matulková I, Nižňanský D, Ardu A, Cannas C, Mantlíková A and Vejpravová 2014 *J. Nanopart. Res.* **16** 1-4
[36] Chen X, Yang Z, Xie Y, Huang Z, Ling L, Zhang S, Pi L, Sun Y and Zhang Y 2013 *J. Appl. Phys.* **113** 17E129
[37] Lock JM 1957 *Proc. Phys. Soc.* B **70** 566
[38] Alshahrani B, ElSaeedy HI, Korna AH, Yakout HA, Maksoud MI, Fahim RA, Gobara M and Ashour AH 2021 *J. Mater. Sci: Mater Electron* **32** 780-97